ISSN (Print) 1226-1750
ISSN (Online) 2233-6656
Journal of Magnetics 30(4), 582-595 (2025) https://doi.org/10.4283/JMAG.2025.30.4.582

Modeling and Design Optimization of an Axial Circumferential E-type Linear Rotary Switched Reluctance Motor

Shuai Xu[1]*, Shuyu Liu[1], Zhenfan Bu[1], Ge Qi[1], Jikai Si[1], Peixin Wang[1], Rui Nie[1], and Guoqiang Han[2]

[1]*School of Electrical and Information Engineering, Zhengzhou University, Zhengzhou 450001, China*
[2]*School of Electrical Engineering, China University of Mining and Technology, Xuzhou 221116, China*

(Received 16 June 2025, Received in final form 18 October 2025, Accepted 20 October 2025)

Accurate modeling and rapid optimal motor design are critical to meet modern industrial requirements while balancing manufacturing burdens. In this paper, an axial circumferential E-type linear rotary switched reluctance motor (ACE-LRSRM) with limited volume, multiple motion modes and high-power density performance is proposed. First, the ACE-LRSRM structure is introduced, and the operation principles of the motor in different modes are analyzed. Afterward, the equivalent magnetic circuit method is introduced to improve the parameter-solving process of the Maxwell tensor method, and a mathematical model of the ACE-LRSRM is established to analyze the electromagnetic characteristics of the motor in linear and nonlinear cases. Additionally, Technique for Order of Preference by Similarity to Ideal Solution is used to optimize the multiobjective design of the motor and improve its target performance. Finally, the validity of the modeling and design optimization of the ACE-LRSRM is verified through comparative finite element analysis.

Keywords : linear rotary motor, switched reluctance motor, improved Maxwell tensor method, equivalent magnetic circuit method, multiobjective optimization

1. Introduction

Multidegree-of-freedom drive technology represents an advanced actuation approach engineered to improve kinematic flexibility, operational efficiency, and structural integration, thereby addressing the demands of complex application scenarios. Linear rotary motion constitutes a prevalent modality within multidegree-of-freedom systems and is extensively utilized in domains such as computer numerical control machine tools, robotic end-effectors, precision assembly and handling equipment, 3D printing, and laser processing. Historically, achieving combined linear rotary motion typically involved mechanical coupling of linear and rotary drive units via intermediate transmission structures, as shown in Fig. 1. Although this conventional configuration fulfilled basic motion requirements, it inherently compromised system compactness and incurred significant transmission losses. In contrast, linear rotary motors (LRMs) eliminate the need for intermediary transmission mechanisms, enabling direct-drive implementation of concurrent linear and rotary motion. This paradigm delivers superior control precision and accelerated dynamic response, leading to its extensive deployment in drilling robotics, artificial heart pumps, renewable energy generation systems, and photovoltaic tracking mechanisms [1-4].

LRMs can be classified into induction, permanent magnet (PM) and reluctance types according to the operating principle of the motor. In [5], a stator-split induction-type LRM was proposed; the stator of this LRM consisted of a curved structure at both ends, and the mover adopted a solid copper-plated structure, which was able to flexibly drive the load for multidimensional motion. However, the coupling effect of the end magnetic

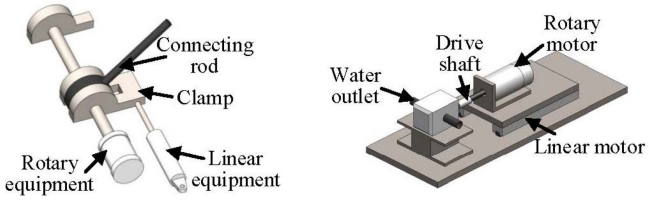

Fig. 1. (Color online) Mechanically coupled linear rotary drive device with intermediate transmission structure.

*Corresponding author: Tel: +15062124092
e-mail: xszzu2020@zzu.edu.cn

field strongly affects the force and torque performance [6]. In [7], a flux-modulated PM-type LRM was proposed. In this LRM, a dual-PM-modulated vernier structure was designed to increase the air-gap magnetic field density and improve the motor force and torque performance. However, the radial segmented linear unit and rotary unit reduce motor integration. In [8], a reluctance-type LRM with an axially staggered stator and axially toothed mover was proposed. The width was varied to realize different motion modes by controlling the alternating conduction of different phases for torque or force cancellation. However, this principle makes designing the parameters of the mover to balance the performance of the linear and rotary units more difficult. In [9], a U-shaped modular reluctance-type LRM was proposed, which was shown to achieve high power density. However, the performance of both linear and rotary units is closely related to the radial modular arrangement of the stator, which increases the size of the motor.

Scholars have proposed numerous approaches to address the problems associated with modeling and the optimal design of motors. Commonly used methods for motor modeling include finite element analysis (FEA), the equivalent magnetic circuit (EMC) and the analytical method. FEA is the most commonly used method but increases the time burden of performance analysis, especially for large 3D FEA. In [10], the effects of the PM deflection angle on the force and torque performance of a PM-type LRM were determined by 3D FEA. Despite the well-established physical principles of EMCs, the limitations inherent to this methodology in addressing leakage flux restrict its applicability for analyzing motor optimization performance. In [11], a tubular reluctance-type LRM with an EMC model was developed to derive the motor inductance and flux linkage characteristics. The analytical method involves a reliable analysis process with high accuracy. On the basis of FEA [12], developed a computationally efficient LRM analytical model that satisfies accuracy requirements. In [13], an algorithm based on the motor phase inductance profile to couple the linear and rotary units of the LRM. In [14], the H-equation and Laplace equation were used to resolve the magnetic field distribution in the proposed induction-type LRM conductor and air gap, and the accuracy of the calculations was verified. To adapt to the development of motors, optimization algorithms have also been implemented from single to multiobjective methods. In [15], the Grey Wolf algorithm was applied to determine the ideal opening and closing angles of a switched reluctance motor. In [16], a method combining particle swarm optimization with the optimal third-order response surface model was proposed, which reduced the burden of motor optimization. In [17], a proxy model based on multi-objective differential evolution and a sorting mutation operator was applied to the proposed linear motor to optimize the force, force ripple, and efficiency of the motor. In [18], a multiobjective Grey Wolf Optimizer was developed to increase the force and reduce the flux saturation. In [19], the optimization scheme of the hierarchical response surface method was compared with the improved multiobjective genetic optimization algorithm to achieve the optimal performance improvement of the motor. In [20], the nondominated sorting genetic algorithm II coupled with response surface methodology and a sensitivity analysis combined approach were proposed to optimize the LRM in a power-oriented manner.

In this paper, an axial circumferential E-type linear rotary switched reluctance motor (ACE-LRSRM) with the following innovations is proposed:

(1) A feasibility proven ACE-LRSRM with high space utilization, high power density, and multiple degrees of freedom operational modes is proposed; in this ACE-LRSRM, the linear unit and the rotary unit are magnetically independent.

(2) An improved Maxwell tensor method (MTM) is proposed, which enables rapid analysis of the flux linkage, radial force, torque and force of the motor under the condition of meeting the accuracy requirements.

(3) The Technique for Order of Preference by Similarity to Ideal Solution(TOPSIS) method is applied to optimize the ACE-LRSRM and improve the overall performance when compared with the use of local optimization.

The sections of this paper are organized as follows. Section II introduces the ACE-LRSRM structure and operating principle. In Section III, the improved MTM is introduced to analyze the performance of the motor. In Section IV, TOPSIS multiobjective parameter optimization is performed to improve the overall motor performance. Section V verifies the feasibility of the modeling and design optimization of the motor and presents the conclusions of the paper.

2. ACE-LRSRM Motor Structure and Operating Principle

2.1. Topology of the ACE-LRSRM

As illustrated in Fig. 2, the ACE-LRSRM employs a dual-drive structure comprising a linear unit and a rotary unit, featuring dual concentric stators and a shared mover. Structural representations and exploded views of the motor are given in Fig. 2(a) and Fig. 2(b), respectively.

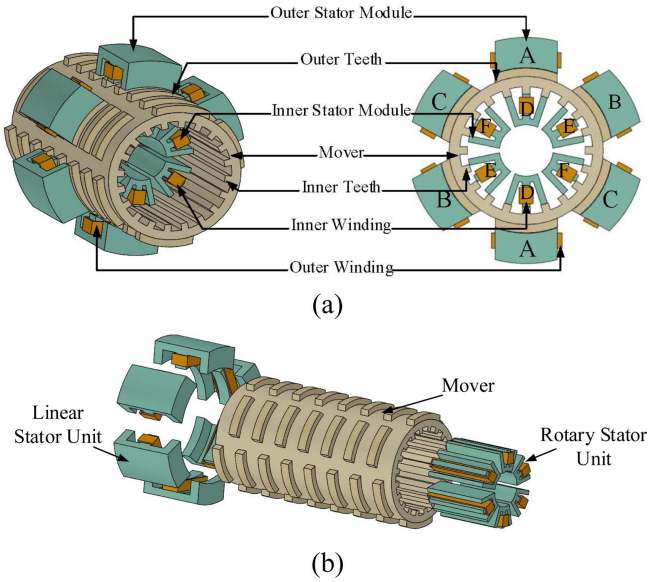

Fig. 2. (Color online) ACE-LRSRM basic structure diagram. (a) Structure diagram. (b) Exploded view.

The outer and inner stators of the ACE-LRSRM have differently oriented E-modules, which correspond to the axial and circumferential distributions of the teeth of the mover. Each stator module integrates a centralized winding on its center pole. The mover assembly comprises three primary components: outer teeth, inner teeth, and a yoke. The inner teeth are uniformly distributed circumferentially, whereas the outer teeth configuration consists of three tooth groups arranged in staggered axial alignment with 60° circumferential phase displacement between adjacent groups and an axial shift equivalent to one outer tooth length. The dimensions of the motor are shown in Fig. 3, while the initial dimension parameters of the ACE-LRSRM are listed in Table 1.

2.2. Principle of operation of the ACE-LRSRM

The ACE-LRSRM achieves multidegree-of-freedom motion through variable reluctance principles, with operational modes encompassing linear, rotary, and helical motions. To accurately describe magnetic circuit changes in different operational modes, the ACE-LRSRM is semicircularly unfolded, as shown in Fig. 4.

As shown in Fig. 4, movement in linear and rotary modes can be achieved by alternately energizing the linear/rotary unit windings. In this case, a single linear

Table 1. ACE-LRSRM initial dimensioning parameters.

Structural parameters	Notes	Initial size
D_{os}	Motor outer diameter	220 mm
l_{os}	Axial length of outer stator	92 mm
l_{is}	Inner stator axial length	92 mm
D_{shaft}	Shaft diameter	50 mm
D_{mo}	Outer diameter of mover	162 mm
l_m	Mover length	299 mm
g_1	Rotary unit air gap	0.3 mm
g_2	Linear unit air gap	0.5 mm
l_{ot}	Axial length of the outer teeth of the mover	13 mm
h_m	Difference between the inner and outer diameters of mover	25 mm
h_{my}	Yoke thickness	10 mm
h_{it}/h_{ot}	Ratio of inner and outer mover tooth height	0.875
l_{osp1}	Axial length of outer stator center pole	15 mm
l_{osp2}	Outer stator side pole axial length	15 mm
h_{osy}	Outer stator yoke thickness	11 mm
w_{os}	Outer stator width	58 mm
w_{ot}	Outer tooth width	60 mm
w_{it}	Inner tooth width	6.8 mm
w_{isp1}	Inner stator center pole width	7 mm
w_{isp2}	Inner stator side pole width	7 mm
h_{isy}	Inner stator yoke thickness	6.5 mm
θ_{is}	Angle difference between inner stator center pole and side pole	18°

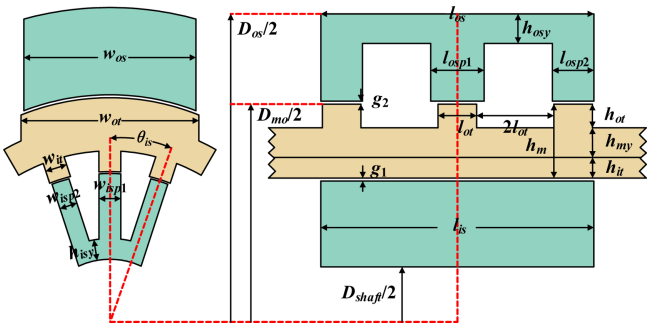

Fig. 3. (Color online) ACELR-SRM motor structure dimensioning.

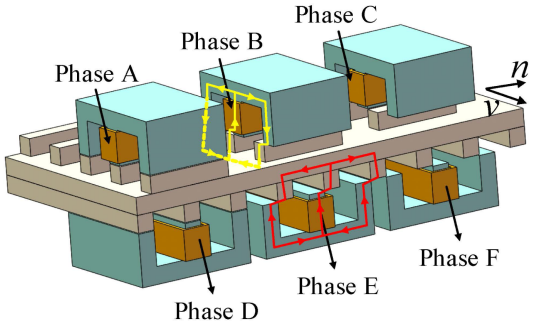

Fig. 4. (Color online) ACE-LRSRM motor operation schematic diagram.

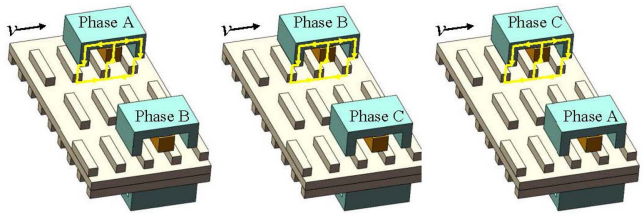

Fig. 5. (Color online) Linear motion principle diagram under axial position changes.

movement requires the cooperation of the rotary position to determine the energized phase, whereas rotary movement does not. As shown in Fig. 5, without considering the change in the rotary motion position, the linear stator and outer teeth of the mover have a large overlap area, and the phase windings of the linear unit alternate between energization as the axial position changes. The axial position x when only the change in rotary position is considered is shown in Fig. 6(a), where F_a, F_b and F_c represent the forces generated by phases A, B and C, respectively. Owing to the alternating distribution of the outer teeth of the mover around the axis, the change in the circumferential position causes changes in the direction and magnitude of the force; consequently, adjacent phases are also alternatingly energized. Ignoring the influence of the inconsistent width of the outer stator poles, and taking phases A and B as examples, the alternating energization principles of phases A and B are shown in Table 2. Notably, during the change in the circumferential position from θ_{0a} to θ_{0b}, phase C changes from zero force to negative force; thus, it is not discussed here.

3. Mathematical Modeling of the ACE-LRSRM Based on the Improved Maxwell Tensor Method

3.1. Maxwell tensor model

On the basis of the similar structural characteristics of the ACE-LRSRM linear unit and the rotary unit magnetic circuit, the subsequent modeling takes the rotary unit as an example to establish the mathematical model. Because the rotary unit stator is a structurally symmetrical six E-type module and the magnetic circuits are independent of each other, modeling only one E-type module is sufficient.

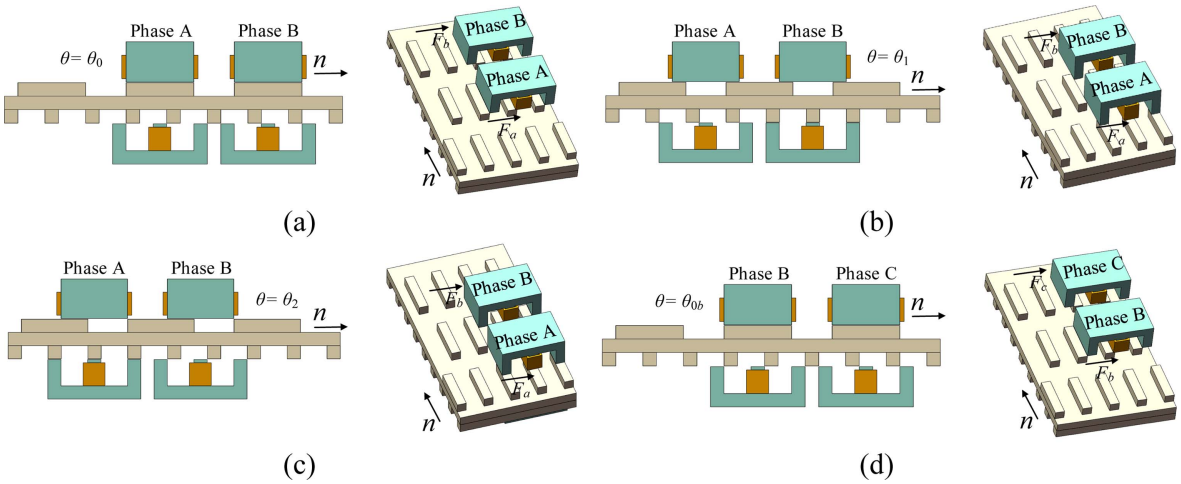

Fig. 6. (Color online) Linear motion principle diagram under circumferential position changes. (a) Phase A energized position. (b) Phase A energized position and phase B start energized position. (c) Phase A stop energized position and phase B energized position. (d) Phase B energized position.

Table 2. Winding energization principle under changes in circumferential position.

Circumferential position	Positional meaning	Energization phase
θ_{0a}	Phase A circumferential alignment position	Phase A
θ_{0a}-θ_1	F_a is positive and F_b is negative.	Phase A
θ_1	F_b equals zero	Phase A
θ_1-θ_2	F_a and F_b are positive	Phase A and B
θ_2	F_a equals zero	Phase B
θ_2-θ_{0b}	F_a equals zero and F_b is positive.	Phase B
θ_{0b}	Phase B circumferential alignment position	Phase B

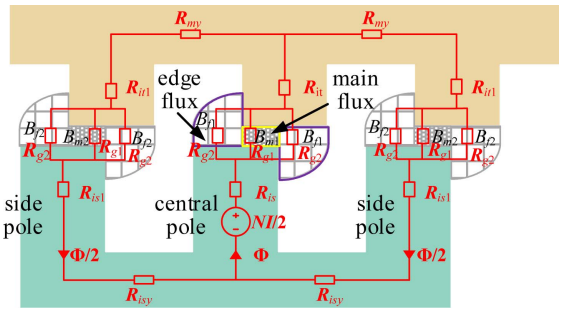

Fig. 7. (Color online) Maxwell Tensor method of integrating paths and equivalent magnetic circuit.

The MTM equates the combined forces and moments within a given volume of magnetic mass to the combined forces of the tensors on the S-plane enclosing the V-surface. The radial and tangential forces are calculated as follows:

$$F_n = \frac{1}{2\mu_0}\iint_S (B_n^2 - B_t^2)dA \tag{1}$$

$$F_t = \frac{1}{\mu_0}\iint_S B_n^2 B_t^2 dA \tag{2}$$

The MTM integration paths and EMC diagrams for the center pole of the E-type stator module and the corresponding kinematic teeth are shown in Fig. 7, whereas the remaining two stator block side pole integration paths are the same as the center pole. To simplify the calculation, the following assumptions need to be made:

(1) The three poles of an E-type stator block are assumed to have approximately the same width as the moving tooth in the circumferential and axial directions.

(2) The air-gap main flux is rectangular, the edge flux consists of a rectangle as well as a quarter-circle, and the magnetic densities are of the same magnitude in the same main flux or edge flux region.

(3) The leakage flux, hysteresis loss and eddy current loss are neglected, and the mutual inductance of the windings between phases is neglected.

According to the integration path shown in Fig. 7, the volume fractions in Equations (1) and (2) are converted to an area fraction according to the assumed conditions, which gives the magnitude of the radial and tangential forces F_{r1} and F_{t1}, respectively, on the center pole of the stator:

$$\begin{aligned} F_{r1} &= l_{is}\left(\int_2^3 B_{m1}^2 dl + \int_4^5 B_{m1}^2 dl + \int_5^6 B_{f1}^2 dl\right)/2\mu_0 \\ &= l_{is}[B_{m1}^2(l_{23}+l_{45}) + B_{f1}^2 l_{56}]/2\mu_0 \end{aligned} \tag{3}$$

$$\begin{aligned} F_{t1} &= l_{is}\left(\int_1^2 B_{f1}^2 dl - \int_3^4 B_{m1}^2 dl\right)/2\mu_0 \\ &= l_{is}(B_{f1}^2 l_{12} - B_{m1}^2 l_{34})/2\mu_0 \end{aligned} \tag{4}$$

where B_{m1}/B_{f1} and B_{m2}/B_{f2} are the main/edge flux densities of the stator center pole and the stator side poles, respectively. μ_0 is the air permeability. l_{12}, l_{23}, l_{34}, l_{45}, and l_{56} are the lengths corresponding to the corresponding integration paths.

Similarly, both sides of the stator pole are subjected to the same radial force and tangential force, and the radial force F_{r2} and tangential force F_{t2} on a particular side tooth are defined as follows:

$$F_{r2} = l_{is}[B_{m2}^2(l_{23}+l_{45}) + B_{f2}^2 l_{56}]/2\mu_0 \tag{5}$$

$$\begin{aligned} F_{t2} &= l_{is}\left(\int_1^2 B_{f2}^2 dl - \int_3^4 B_{m2}^2 dl\right)/2\mu_0 \\ &= l_{is}(B_{f2}^2 l_{12} - B_{m2}^2 l_{34})/2\mu_0 \end{aligned} \tag{6}$$

When two stator blocks of one phase are energized simultaneously, the radial force on the mover will cancel out, and the radial force on the mover when one of the stator block windings is energized is:

$$F = F_{r1} + 2F_{r2}\cos\frac{180\beta}{\pi} \tag{7}$$

where β is the step angle of the mover inner teeth.

Because one phase contains two stator blocks, the electromagnetic torque on the mover when the winding of one phase of the rotary unit is energized can be derived as follows:

$$T = 2(F_{t1} + 2F_{t2})\frac{D_{mi}}{2} \tag{8}$$

where D_{mi} is the rotary unit armature diameter.

The length of each integration path is expressed in the following equation:

$$\begin{cases} l_{12} = g_1 + \dfrac{D_{mi}}{2}\left(\dfrac{\beta}{2} - \theta\right) \\ l_{34} = g_1 \\ l_{23} + l_{45} = \dfrac{D_{mi}}{2}\left(\alpha - \dfrac{\beta}{2} + \theta\right) \\ l_{56} = \dfrac{D_{mi}}{2}\left(\dfrac{\beta}{2} - \theta\right) \end{cases} \tag{9}$$

where α is the stator pole and stator tooth angle and θ is the stator pole and stator tooth relative angle.

The magnetic flux Φ through the stator center pole can

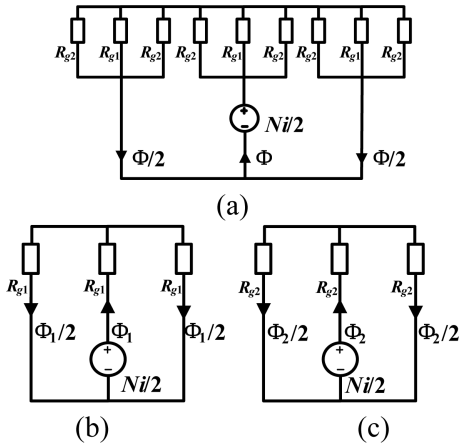

Fig. 8. Linear EMC diagram of rotary unit. (a) EMC. (b) EMC about the main flux. (c) EMC about the edge flux.

be expressed by the following formula:

$$\Phi = B_{m1}S_m + 2B_{f1}S_f \tag{10}$$

where S_m is the equivalent cross-sectional area of the main air gap at the stator center pole and S_f is the cross-sectional area of the air gap at the edge of the stator center pole.

The flux linkage through one phase of the stator can be expressed as follows:

$$\Psi = N_R\Phi \tag{11}$$

where N_R is the number of turns of a phase winding.

3.2. Air gap magnetic density solution

(1) Linear model

In the linear case, the iron core is not saturated, and the core reluctance is much smaller than the air-gap reluctance; thus, the core reluctance is completely ignored in the model. The EMC of the rotary unit is shown in Fig. 8. According to the principle of circuit superposition, as the magnetic flux moves through two branches, the main flux branch and the edge flux branch; Fig. 8(a) is equivalent to Fig. 8(b) and Fig. 8(c).

The flux before equivalence is related to the main flux Φ_1 and edge flux Φ_2 after equivalence as follows:

$$\Phi = \Phi_1 + \Phi_2 \tag{12}$$

According to the EMC diagram, the main flux densities are calculated with the following equation when neglecting leakage:

$$\begin{cases} \dfrac{N_R i_R}{2} = \Phi_1 \dfrac{3R_{g1}}{2} \\ \Phi_1 = B_{m1}S_m \\ R_{g1} = \dfrac{g_1}{\mu_0 S_m} \end{cases} \tag{13}$$

where R_{g1} is the main flux reluctance of the center tooth.

Similarly, the edge flux densities are calculated using the following equation:

$$\begin{cases} \dfrac{N_R i_R}{2} = \Phi_2 \dfrac{3R_{g2}}{4} \\ \Phi_2 = 2B_{f1}S_f \\ R_{g2} = \dfrac{l_f}{\mu_0 S_f} \end{cases} \tag{14}$$

where R_{g2} is one of the two edge flux resistances of the center tooth and l_f is the average length of the edge flux, denoted as follows:

$$l_f = g_1 + \frac{2\pi\frac{D_{mi}}{2}(\frac{\beta}{2}-\theta)}{4}\frac{1}{2} = g_1 + \frac{\pi D_{mi}(\beta-2\theta)}{16} \tag{15}$$

From Equation (16), the main flux air-gap densities B_{m1} and edge densities B_{f1} of the center tooth and the main flux densities B_{m2} and edge densities B_{f2} of the side teeth are obtained as follows :

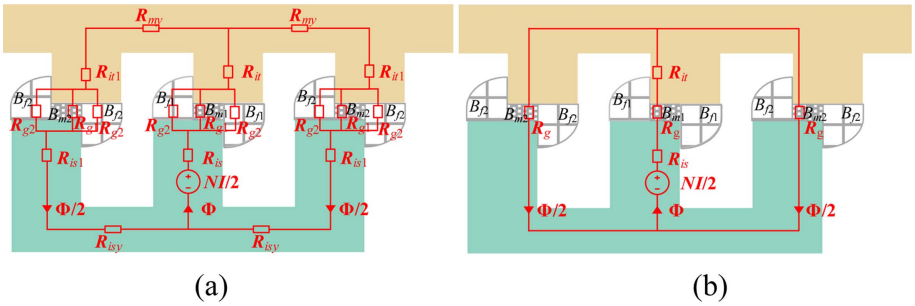

Fig. 9. (Color online) Nonlinear EMC diagram of rotary unit. (a) Oversaturation condition. (b) Saturated condition.

$$\begin{cases} B_{m1}=\dfrac{\mu_0 N_R i_R}{3g_1} \qquad B_{m2}=\dfrac{1}{2}B_{m1} \\ B_{f1}=\dfrac{\mu_0 N_R i_R}{3(g_1+\dfrac{\pi D_{mi}(\beta\text{-}2\theta)}{16})} \qquad B_{f2}=\dfrac{1}{2}B_{f1} \end{cases} \tag{16}$$

(2) Nonlinear model

In the nonlinear case, the saturated core reluctance is large and not negligible. Because oversaturation produced by excessive current is more damaging to the motor, the saturation case at excessive current is not considered. In accordance with the design principle and structural distribution of the motor, the region of the stator block center pole and the corresponding moving teeth are first to saturate as the current increases. Therefore, in the calculation, only the reluctance of the stator block center pole and the corresponding mover tooth is retained, whereas the others are ignored; thus, the EMC of the rotary unit is shown in Fig. 9(b).

The simplified EMC equation for the rotary unit is as follows:

$$\frac{N_R I_R}{2}=\Phi(R_{it}+R_{is}+\frac{3}{2}R_g) \tag{17}$$

where I_R is the winding current, R_{it} is the stator tooth reluctance, R_{is} is the stator center tooth reluctance, and R_g is the total air gap reluctance.

The total air gap reluctance R_g can be expressed by the following equation:

$$\frac{1}{R_g}=\frac{1}{R_{g1}}+\frac{2}{R_{g2}} \tag{18}$$

The equivalent cross-sectional area of the main air gap and the marginal air gap is given by the following equation:

$$\begin{aligned} S_m&=(\alpha-\frac{\beta}{2}+\theta)\frac{D_{mi}l_{is}}{2} \\ S_f&=(\frac{\beta}{2}-\theta)\frac{D_{mi}l_{is}}{2} \end{aligned} \tag{19}$$

Associations (13), (16) and (19) yield the following expressions for the main air-gap reluctance and the edge air-gap reluctance at different positions:

$$\begin{aligned} R_{g1}&=\frac{2l_f}{\mu_0(\alpha-\frac{\beta}{2}+\theta)D_{mi}l_{is}} \\ R_{g2}&=\frac{2l_f}{\mu_0(\frac{\beta}{2}-\theta)D_{mi}l_{is}} \end{aligned} \tag{20}$$

The core reluctance at the stator center tooth can be expressed by the following equation:

$$R_{is}=\frac{h_{is}}{\mu_s S_s} \tag{21}$$

where h_{is} is the stator center tooth height, S_s is the stator center tooth equivalent cross-sectional area, and μ_s is the stator core permeability.

Because the shape of the flux through the stator is related mainly to the degree of overlap of the stator and mover teeth, when the shape of the flux through the core is assumed to be trapezoidal, the equivalent flux area is expressed by the following equation:

$$S_s=(4\alpha-\frac{\beta}{2}+\theta)\frac{D_{mi}l_{is}}{4} \tag{22}$$

The core reluctance at the mover teeth can be expressed by the following equation:

$$R_{it}=\frac{h_{it}}{\mu_t S_t} \tag{23}$$

where h_{it} is the height of the mover inner tooth, S_t is the equivalent cross-sectional area of the kinematic tooth flux, and μ_t is the kinematic tooth permeability.

On the basis of the previous assumption that the width of the stator moving teeth is the same, the equivalent flux

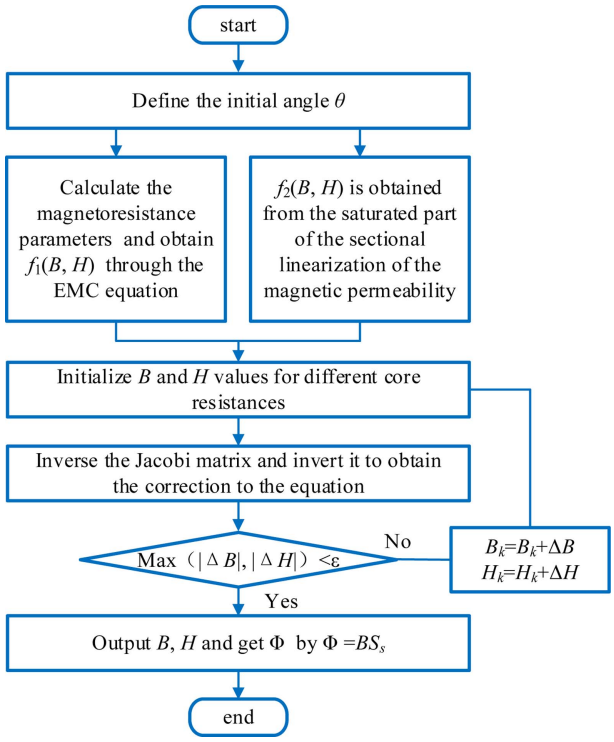

Fig. 10. (Color online) Newton Raphson method iteration flowchart.

area and permeability of the stator and moving teeth are the same:

$$S_t = S_s \qquad \mu_t = \mu_s \tag{24}$$

Simplifying under the previous assumptions, only μ_s is unknown at this point. Using the Newton-Raphson method, the solution of this problem is equated to a system of nonlinear equations by substituting Equation (21), (23) and (24) into the equations of the EMC diagram and organizing them to obtain the following equation:

$$\frac{N_R I_R}{2} = \Phi[\frac{(h_{it}+h_{is})}{\mu_s S_s} + \frac{3}{2}R_g] \tag{25}$$

The main flux Φ through the center pole of the stator can also be expressed by the following equation:

$$\Phi = B_s S_s \tag{26}$$

where B_s is the stator center pole density.

The permeability of the stator center pole can be expressed as follows:

$$\mu_s = \frac{B_s}{100 H_s} \tag{27}$$

where H_s is the magnetic field strength (A/cm) of the stator center pole and the corresponding moving teeth.

Substituting Equations (26) and (27) into Equation (25) and organizing yields the EMC equations as follows:

$$100(h_{is}+h_{it})H_s + \frac{3}{2}R_g B_s H_s - \frac{N_R I_R}{2} = 0 \tag{28}$$

A second equation for the relationship between B and H is obtained on the basis of the magnetization curve. By fitting the nonlinear part of the magnetization curve of the core material in segments, the expression obtained from the fifth-order fitting is as follows:

$$H = A_1 B^5 + A_2 B^4 + A_3 B^3 + A_4 B^2 + A_5 B + C \tag{29}$$

At this point, the solution of the EMC is equivalent to the joint solution of B_s and H_s for Equations (28) and (29).

The solution flow of the Newton-Raphson method is shown in Fig. 10. After the Newton-Raphson method is used to determine the magnetic flux, the stator center teeth of the main air gap magnetic density and edge air gap magnetic density can be expressed as follows:

$$B_{m1} = \frac{0.5R_{g2}\Phi}{(R_{g1}+0.5R_{g2})S_m} \qquad B_{f1} = \frac{0.5R_{g1}\Phi}{(R_{g1}+0.5R_{g2})S_f} \tag{30}$$

4. Multiobjective Optimization of a Motor Based on the Topsis Method

Because the initial structural dimensioning of the ACE-LRSRM is based on some preliminary assumptions and empirical formulas, the performance specifications at the beginning of the motor design may conflict with each other in practical applications. Performance needs to be improved by multiobjective optimization of the motor structural parameters, and the optimization objectives of the ACE-LRSRM are selected to be the average force (F_{av}), force ripple (R_F), linear winding copper consumption (P_{cu1}), average torque (T_{av}), torque ripple (R_T) and rotary winding copper consumption (P_{cu2}).

4.1. Sensitivity analysis and weighting parameter calculation

The general sensitivity index is used to assess the sensitivity of the design variables to the optimization object, and the single factor sensitivity is expressed as follows:

$$S(n_i) = \frac{\partial f(n_i)}{\partial n_i} = \frac{\Delta f(n_i)/f(n_i)}{\Delta n_i / n_i} \tag{31}$$

where n_i is the i_{th} scenario for a certain structural parameter and $f(n_i)$ is the corresponding performance optimization index when the structural parameter is n_i.

On the basis of the influence of each structural

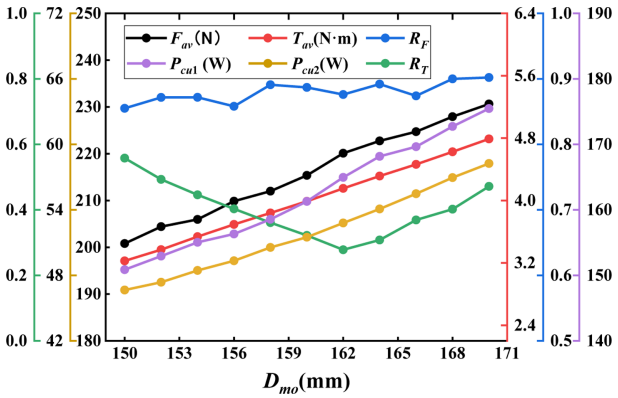

Fig. 11. (Color online) Plot of target performance variation under different D_{mo} schemes.

parameter of this motor structure on the performance of the linear unit and the rotary unit, the multifactor sensitivity analysis is stratified according to the motor structure. The first layer of structural parameters D_{mo}, h_{my} and target performance [F_{av}, R_F, P_{cu1}, T_{av}, R_T, P_{cu2}] affect the performance of both linear and rotary units; the second layer of structural parameters h_{osy}, l_{osp1}, l_{osp2}, and w_{os} affects the performance of the linear unit and target performance [F_{av}, R_F, P_{cu1}]; the third layer of structural parameters h_{isy}, w_{isp1}, w_{isp2}, and w_{it} affects the performance of the rotary unit and target performance [T_{av}, R_T, P_{cu2}]. Then, the multifactor sensitivity of these three layers can be expressed as follows:

$$\begin{cases} G(n_i)=\lambda_{11}\left|S_{F_{av}}\right|+\lambda_{12}\left|S_{R_F}\right|+\lambda_{13}\left|S_{P_{cu1}}\right| \\ \qquad +\lambda_{14}\left|S_{T_{av}}\right|+\lambda_{15}\left|S_{R_T}\right|+\lambda_{16}\left|S_{P_{cu2}}\right| \text{ (First layer)} \\ G(n_i)=\lambda_{21}\left|S_{F_{av}}\right|+\lambda_{22}\left|S_{R_F}\right|+\lambda_{23}\left|S_{P_{cu1}}\right| \text{ (Second layer)} \\ G(n_i)=\lambda_{31}\left|S_{T_{av}}\right|+\lambda_{32}\left|S_{R_T}\right|+\lambda_{33}\left|S_{P_{cu2}}\right| \text{ (Third layer)} \end{cases} \tag{32}$$

where S_X (where X is the optimization objective) is the one-factor sensitivity of a structural parameter to X. λ_{mn} is the multifactor sensitivity weight coefficient for different structural parameters and is defined as follows:

$$\sum_{j=1}^{n}\lambda_{aj}=1 \quad a=1,\ 2,\ 3 \tag{33}$$

Entropy is used to measure the degree of uncertainty or chaos of a system, and in a multiobjective system, the weight of a factor should directly correlate with its influence on the decision-making result. Using the information entropy weighting method, the decision matrix for a certain structural parameter was obtained from the FEA results as follows:

$$D=\begin{bmatrix} x_{11} & x_{12} & \cdots & x_{1n} \\ x_{21} & x_{22} & \cdots & x_{2n} \\ \vdots & \vdots & \vdots & \vdots \\ x_{m1} & x_{m2} & \cdots & x_{mn} \end{bmatrix} \tag{34}$$

where x_{ij} refers to the j_{th} optimization objective performance corresponding to the i_{th} solution for a given structural parameter.

The total contribution of all programs to the j_{th} indicator, E_j, is calculated with the following equation:

$$E_j=-\frac{1}{\ln(m)}\sum_{i=1}^{m}\frac{x_{ij}}{\sum_{i=1}^{m}x_{ij}}\ln\left(\frac{x_{ij}}{\sum_{i=1}^{m}x_{ij}}\right) \tag{35}$$

$$w_j=(1-E_j)/\sum_{j=1}^{n}(1-E_j) \tag{36}$$

$$\lambda_{aj}=\lambda_j w_j/\sum_{j=1}^{n}\lambda_j w_j \tag{37}$$

where w_j is the objective weight of the performance of the j_{th} optimization objective, λ_j is the subjective weight coefficient, and λ_{aj} is the final weight coefficient.

Under the unified simulation environment, FEA dynamic simulation is carried out for each optimization parameter. For example, the single-factor sensitivity to the target performance is obtained through Equation (31) as shown in Fig. 11, and is the same for the remaining parameters. On the basis of the obtained single-factor sensitivity data of each optimization parameter, the final weight coefficients are obtained by the information entropy method mentioned above in Table 3. Multifactor sensitivity analysis of each optimization parameter is subsequently carried out on the basis of Equation (32), as shown in Fig. 12. Fig. 12(a) shows that $G(D_{mo})>G(h_{my})$; therefore, D_{mo} should be optimized first in the multifactor optimization, followed by h_{my}.

Table 3. Weighting factors for different structural parameters.

Structural parameters	Objective weights	Final weights
D_{mo}	[0.029, 0.004, 0.036, 0.228, 0.623, 0.080]	[0.053, 0.002, 0.080, 0.408, 0.278, 0.179]
h_{my}	[0.347, 0.164, 0.188, 0.050, 0.233, 0.018]	[0.460, 0.054, 0.312, 0.066, 0.078, 0.030]
h_{osy}	[0.649, 0.052, 0.299]	[0.627, 0.012, 0.361]
l_{osp1}	[0.073, 0.334, 0.593]	[0.082, 0.093, 0.825]
l_{osp2}	[0.014, 0.827, 0.159]	[0.034, 0.494, 0.472]
w_{os}	[0.022, 0.009, 0.969]	[0.018, 0.002, 0.980]
h_{isy}	[0.200, 0.720, 0.080]	[0.417, 0.375, 0.208]
w_{isp1}	[0.178, 0.215, 0.607]	[0.180, 0.054, 0.766]
w_{isp2}	[0.086, 0.744, 0.170]	[0.177, 0.384, 0.439]
w_{it}	[0.307, 0.330, 0.363]	[0.364, 0.098, 0.538]

4.2. TOPSIS multiobjective optimization

TOPSIS is a multiobjective decision-making method that is based on the theory of similarity and determines the optimal solution by comparing the similarity between alternatives and the ideal solution.

The performance parameters of some of the optimization objectives (R_F, P_{cu1}, R_T and P_{cu2}) in the decision matrix of Equation (34) are normalized to obtain the matrix Z as shown in Equation (38):

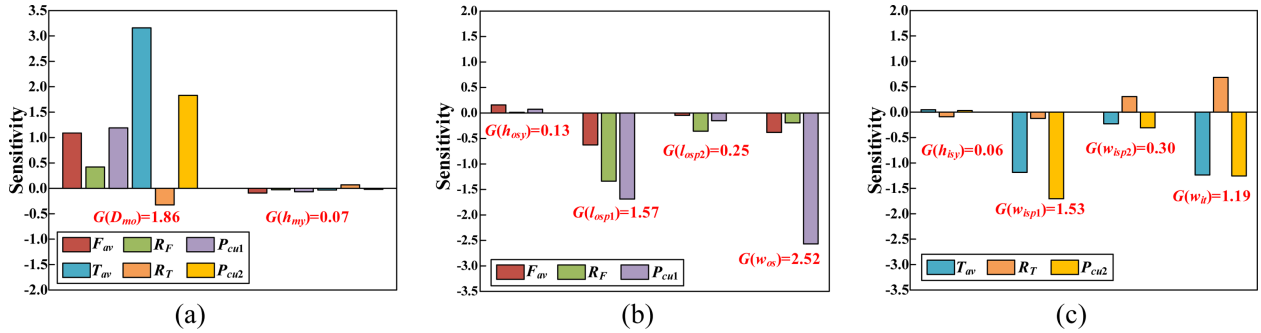

(a) (b) (c)

Fig. 12. (Color online) Structural parameter sensitivity histograms. (a) First layer. (b) Second layer. (c) Third layer.

$$\begin{cases} a_{ij} = \max\left\{x_{1j}, x_{2j}, \cdots, x_{mj}\right\} - x_{ij} \\ z_{ij} = \dfrac{a_{ij}}{\sqrt{\sum_{i=1}^{m} a_{ij}^2}} \\ Z_{ij} = \dfrac{z_{ij} - \min\left\{z_{1j}, z_{2j}, \cdots, z_{mj}\right\}}{\max\left\{z_{1j}, z_{2j}, \cdots, z_{mj}\right\} - \min\left\{z_{1j}, z_{2j}, \cdots, z_{mj}\right\}} \end{cases} \tag{38}$$

The maximum and minimum values of each optimization metric of the matrix Z are determined as follows:

$$\begin{cases} Z^+ = \left\{Z_1^+, Z_2^+, \cdots, Z_n^+\right\} \\ \quad = \left\{\max(Z_{11}, \cdots, Z_{m1}), \max(Z_{12}, \cdots, Z_{m2}), \cdots, \max(Z_{1n}, \cdots Z_{mn})\right\} \\ Z^- = \left\{Z_1^-, Z_2^-, \cdots, Z_n^-\right\} \\ \quad = \left\{\min(Z_{11}, \cdots, Z_{m1}), \min(Z_{12}, \cdots, Z_{m2}), \cdots, \min(Z_{1n}, \cdots, Z_{mn})\right\} \end{cases} \tag{39}$$

The final score for the i_{th} program is calculated using (40):

$$S_i = \frac{\sqrt{\sum_{j=1}^{n} w_j (Z_j^- - Z_{ij})^2}}{\sqrt{\sum_{j=1}^{n} w_j (Z_j^+ - Z_{ij})^2} + \sqrt{\sum_{j=1}^{n} w_j (Z_j^- - Z_{ij})^2}} \tag{40}$$

According to the sensitivity analysis results, eleven optimization schemes for the structural parameters D_{mo} are optimized in the first layer, and the scores of each scheme are obtained and ranked by TOPSIS decision scoring through Equations (40)-(42). The three schemes, namely, the best (162 mm), the medium (158 mm), and the worst (150 mm), are selected and made into radar charts for comparison, as shown in Fig. 13(a). On the basis of the evaluation scores of S_1=0.64 (1/11), S_6=0.56 (6/11), and S_{11}=0.39 (11/11), the final size is selected as 162 mm. The radargram of the structural parameter h_{my} obtained through the same process is shown in Fig. 13(b), and the final size of the structural parameter is selected as

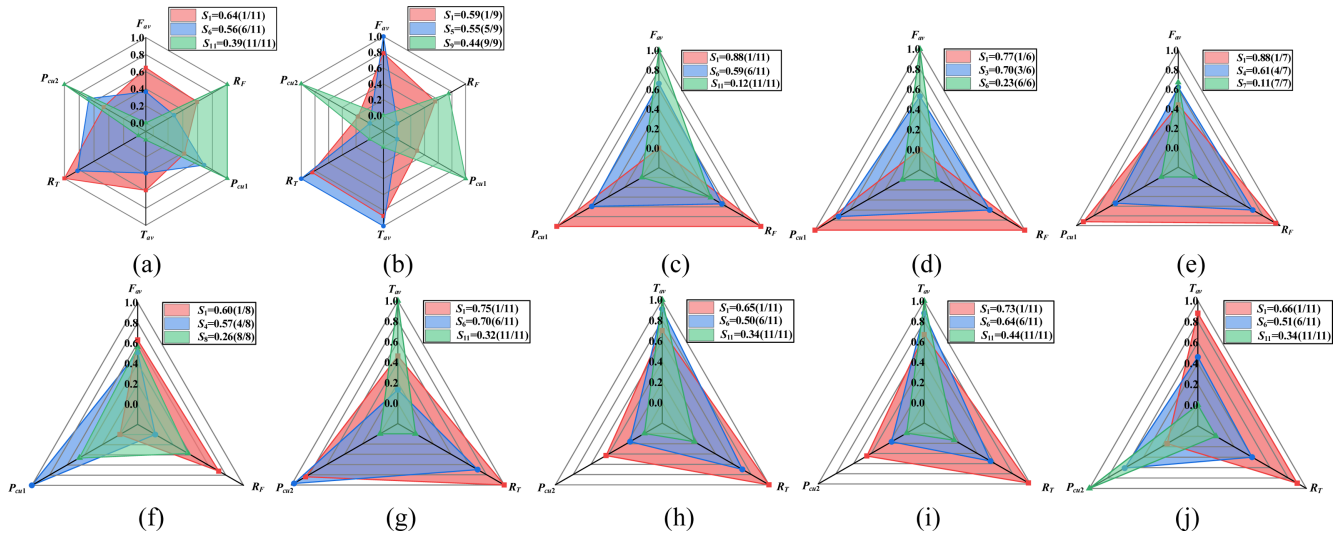

(a) (b) (c) (d) (e)

(f) (g) (h) (i) (j)

Fig. 13. (Color online) Radar charts of the results of decision making on structural parameters. (a) D_{mo}. (b) h_{my}. (c) w_{os}. (d) l_{osp1}. (e) l_{osp2}. (f) h_{osy}. (g) w_{isp1}. (h) w_{it}. (i) w_{isp2}. (j) h_{isy}.

9 mm. Similarly, the radar charts for the second-layer structural parameters [w_{os}, l_{osp1}, l_{osp2}, h_{osy}] and the third-layer parameters [w_{isp1}, w_{it}, w_{isp2}, h_{isy}] are presented in Fig. 13(c)-(f) and Fig. 13(g)-(j), respectively.

5. Analysis of Results

5.1. Feasibility verification of the ACE-LRSRM principle

To verify the feasibility of the motor design, electromagnetic FEA was performed on the linear and rotary units according to the initial structural parameters.

(1) Linear unit

The electromagnetic characteristic curve when a constant current is applied to the winding of the linear unit for one electrical cycle is shown in Fig. 14.

The dynamic electromagnetic characteristic graph of the linear unit under the designed rated voltage and rated speed of motion are shown in Fig. 15. The dynamic force curve is shown in Fig. 15(a); at this point, the average force of the linear unit is 215.64 N, and the force ripple is 88%. The dynamic current curve of the three-phase winding is shown in Fig. 15(b), and the linear unit winding copper consumption is 161.31 W.

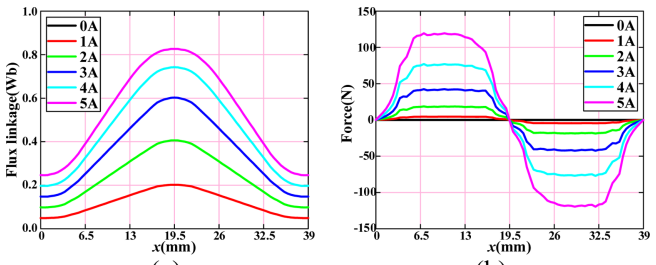

(a) (b)

Fig. 14. (Color online) Static characteristic curve of linear unit. (a) Static flux linkage curve. (b) Static force curve.

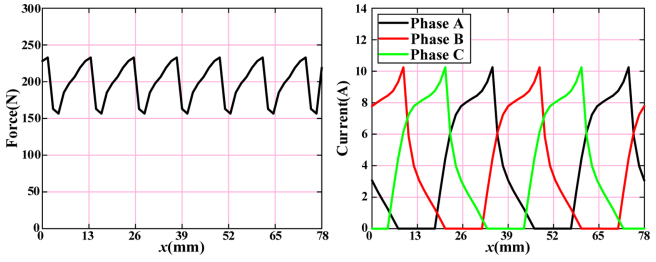

(a) (b)

Fig. 15. (Color online) Dynamic electromagnetic characteristics graphs on linear unit. (a) Dynamic force curve. (b) Dynamic current curve.

(2) Rotary unit

The electromagnetic characteristic curve obtained when a constant current is applied to the winding of the rotary unit for one electrical cycle is shown in Fig. 16. Notably, as shown in Fig. 16(b), the static torque has a flat-topped waveform when the current magnitude ranges from 0 A to 9 A, at which point the rotary unit is more efficient.

The dynamic electromagnetic characteristic graph of the rotary unit rotating at the designed rated voltage and rated speed is shown in Fig. 17. The dynamic torque graph is shown in Fig. 17(a); at this point, the average torque of the rotary unit is 4.00 N·m, and the torque ripple is 33%. The dynamic current curve of the three-phase winding is shown in Fig. 17(b), and the rotary unit winding copper consumption is 51.62 W.

5.2. Verification of the feasibility of the Maxwell tensor model

Following the derivation in Section III, the half-period expressions for the flux linkage, radial force on an individual subblock, rotary unit torque, and linear unit force under single-phase excitation and linear conditions are derived as follows:

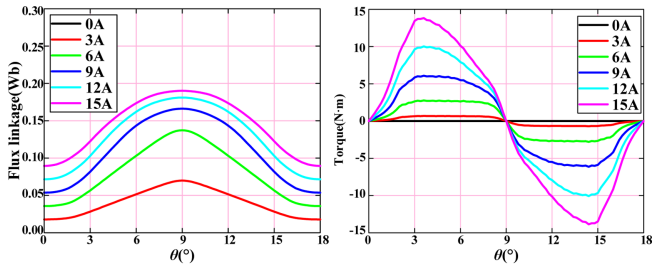

(a) (b)

Fig. 16. (Color online) Static characteristic curve of rotary unit. (a) Static flux linkage curve. (b) Static torque curve.

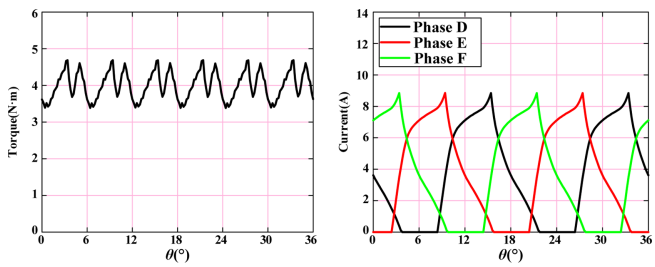

(a) (b)

Fig. 17. (Color online) Dynamic electromagnetic characteristics graphs on rotary unit. (a) Dynamic torque curve. (b) Dynamic current curve.

$$\begin{cases} \Psi_R(\theta,i)=\mu_0 N_R{}^2 i_R D_{mi} l_{is} J_1(\theta) \\ \Psi_L(\theta,x,i)=\mu_0 N_L{}^2 i_L D_{mo} J_2(\theta)(\theta_0-\theta) \\ F(\theta,i)=\mu_0 N_R{}^2 i_R{}^2 D_{mi} l_{is}(2+\cos\dfrac{180\beta}{\pi})J_3(\theta) \\ T(\theta,i)=\mu_0 N_R{}^2 i_R{}^2 D_{mi} l_{is} J_4(\theta) \\ F(\theta,x,i)=\mu_0 N_L{}^2 i_L{}^2 D_{mo} J_5(\theta)(\theta_0-\theta) \end{cases} \quad (41)$$

where N_L is the number of turns per linear unit; i_R is the current carried by the linear element; θ_0 represents the circumferential pole arc of the linear stator; and $J_1(\theta)$, $J_2(\theta)$, $J_3(\theta)$, $J_4(\theta)$ and $J_5(\theta)$ are as follows:

$$\begin{cases} J_1(\theta)=\dfrac{2\alpha-\beta+2\theta}{12g_1}+\dfrac{8(\beta-2\theta)}{48g_1+3\pi D_{mi}(\beta-2\theta)} \\ J_2(\theta)=\dfrac{2l_{osp}-L+2x}{12g_2}+\dfrac{4(L-2x)}{24g_2+\pi(L-2x)} \\ J_3(\theta)=\dfrac{2\alpha-\beta+2\theta}{144g_1^2}+\dfrac{\beta-2\theta}{18[16g_1+\pi D_{mi}(\beta-2\theta)]^2} \\ J_4(\theta)=\dfrac{192g_1+48D_{mi}(\beta-2\theta)}{9[16g_1+\pi D_{mi}(\beta-2\theta)]^2}-\dfrac{1}{12g_1} \\ J_5(\theta)=\dfrac{2(2g_2+L-2x)}{3[16g_2+\pi D_{mi}(\beta-2\theta)]^2}-\dfrac{1}{12g_2} \end{cases} \quad (42)$$

where l_{osp} is the axial length of the linear stator and $L/2$ corresponds to the mover displacement required to transition the linear element from the fully unaligned position to the aligned position.

Combined with the nonlinear model solution, the complete waveforms of the flux linkage, radial force, torque and force are obtained and compared with the FEA results, as shown in Figs. 18-22. The errors of the rotary unit flux linkage, linear unit flux linkage, radial force, torque and force are within 5%, 7%, 10%, 7%, and 8%, respectively, under different rotary and linear positions of the improved MTM model, which verifies the validity of the model.

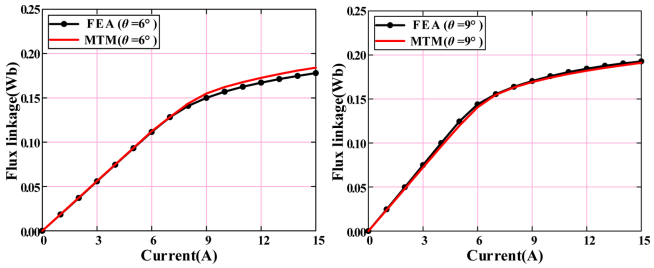

Fig. 18. (Color online) Comparison of rotary unit flux linkage. (a) θ=6°. (b) θ=9°.

5.3. Verification of the feasibility of multiobjective optimization

The parameters of the ACE-LRSRM after TOPSIS

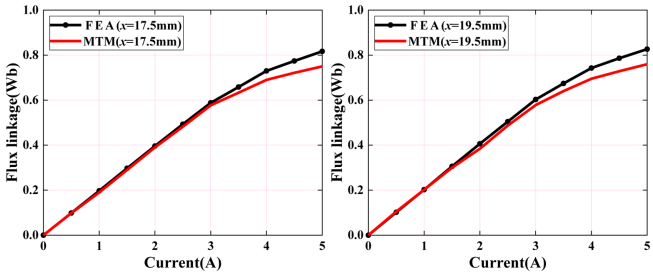

Fig. 19. (Color online) Comparison of linear unit flux linkage. (a) x=17.5 mm. (b) x=19.5 mm.

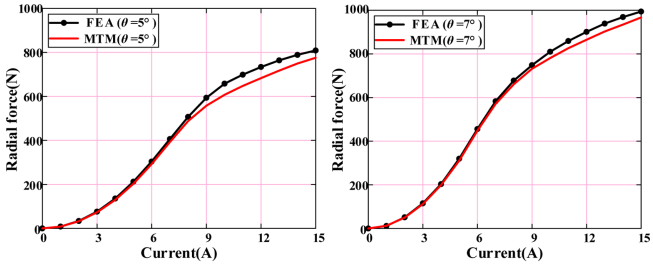

Fig. 20. (Color online) Comparison of radial force. (a) θ=5°. (b) θ=7°.

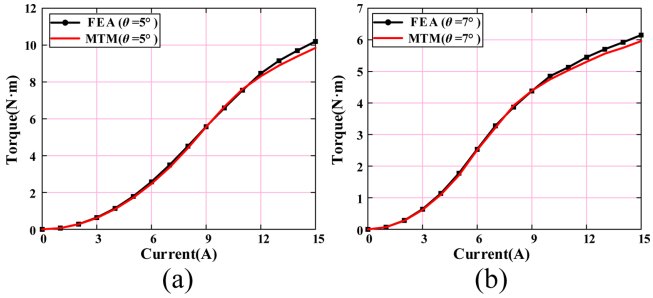

Fig. 21. (Color online) Comparison of torque. (a) θ=5°. (b) θ=7°.

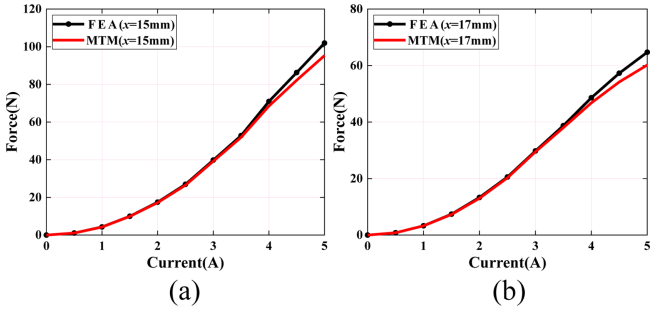

Fig. 22. (Color online) Comparison of force. (a) x=15 mm. (b) x=17 mm.

multiobjective optimization are listed in Table 4, and FEA was performed on the parameters before and after optimization. Additionally, a comparison of the performance before and after optimization is shown in Table 4. For the linear unit, the performance curves before and after optimization are shown in Fig. 23; F_{av} increases from 215.64 N to 225.53 N, which constitutes a 4.58% increase; R_F decreases from 88% to 69%, which constitutes a 21.59% decrease; and P_{cu1} decreases from 161.31 W to 153.61 W, which constitutes a 4.77% decrease. The performance curves for the rotary unit before and after optimization are shown in Fig. 24; T_{av} increased from 4.00 N·m to 5.12 N·m, which is an increase of 28.00%; R_T changed little, and P_{cu2} increased by 30.28%. Despite the increase in P_{cu1}, the main performance T_{av} increases by almost an equal extent; therefore, motor performance can be assumed to be fully optimized.

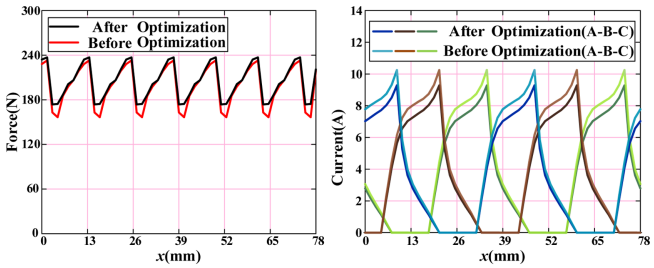

Fig. 23. (Color online) Performance comparison before and after linear unit optimization. (a) Force comparison curve. (b) Current comparison curve.

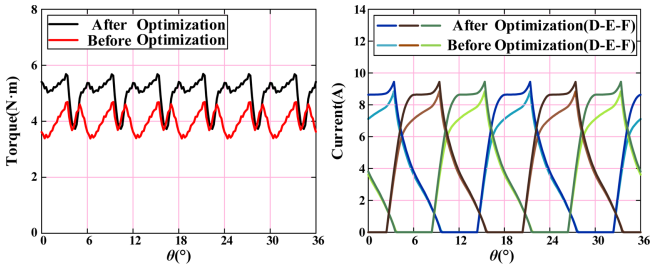

Fig. 24. (Color online) Performance comparison before and after rotary unit optimization. (a) Torque comparison curve. (b) Current comparison curve.

Table 4. Optimization results of ACE-LRSRM parameters.

Structural parameters	Initial size	Final size
l_{osp1}	15 mm	18 mm
w_{it}	6.8 mm	6.6 mm
w_{isp2}	7 mm	5.2 mm
h_{isy}	6.5 mm	7.6 mm

5.4. Conclusion

This paper proposes a viable ACE-LRSRM that is capable of a variety of motion modes and is characterized by high integration, high space utilization and high power density. Moreover, a reliable mathematical model was established for the proposed motor based on the improved MTM; the error of the resulting flux linkage is less than 5%, the error of the torque is less than 7%, and the error of the radial force exerted on the mover is less than 10%. Finally, multiobjective optimization of the motor using the TOPSIS method was carried out to improve the overall performance of the motor. The optimization objective performance [F_{av}, R_F, P_{cu1}, T_{av}, R_T, P_{cu2}] varies as follows: [+4.58%, -21.59%, -4.77%, +28.00%, -3.03%, +30.28%], respectively. Therefore, the effectiveness of the method is verified.

References

[1] K. Guo and Y. Guo, IEEE Trans. Ind. Electron. **71**, 11195 (2024).
[2] R. V. Giuffrida, A. Horat, D. Bortis, T. Bierewirtz, K. Narayanaswamy, M. Granegger, and J. W. Kolar, IEEE Open J. Ind. Electron. Soc. **5**, 359 (2024).
[3] R. Nie, J. Si, Y Jia, P. Wang, S. Xu, J. Liang, and C. Gan, IEEE Trans. Ind. Appl. **60**, 6170 (2024).
[4] Y Zou, KWE Cheng, Energies. **12**, 1983 (2019).
[5] J. Si, H. Feng, L. Ai, Y. Hu, and W. Cao, IEEE Trans. Energy Convers. **30**, 1200 (2015).
[6] L. Xie, J. Si, Y. Hu, H. Feng, and K. Ni, IEEE Trans. Ind. Electron. **67**, 931 (2020).
[7] Y. Ma, S. Niu, W. Fu, and J. Fei, IEEE Trans. Transport.

Table 5. Performance comparison before and after ACE-LRSRM optimization.

ACE-LRSRM	Linear unit			Rotary unit		
Optimized variables	F_{av}	R_F	P_{cu1}	T_{av}	R_T	P_{cu2}
Before optimization	215.64 N	88%	161.31 W	4.00 N·m	33%	51.62 W
After optimization	225.53 N	69%	153.61 W	5.12 N·m	32%	67.25 W
Optimization ratio	+4.58%	-21.59%	-4.77%	+28.00%	-3.03%	+30.28%

Electrific. **11**, 4296 (2025).
[8] S. Xu, X. Jiang, J. Si, R. Nie, and P. Wang, 2023 26th International Conference on Electrical Machines and Systems (ICEMS). Zhuhai, China, (2023) pp. 3666-3671.
[9] H. Chen, X. Wang, C. Liu, M. F. Shamiyev, A. O. Pulatov, and A. Musolino, IEEE Trans Plasma Sci. **53**, 2653 (2025).
[10] O. Dobzhanskyi and R. Gouws, Electr. Eng. **99**, 997 (2017).
[11] H. Chen, X. Wang, C. Liu, A. Musolino, P. Rafajdus, and X. Li, IEEE Trans Plasma Sci. **53**, 2704 (2025).
[12] O. Safdarzadeh, A. Mahmoudi, E. Afjei, and H. Torkaman, IEEE Trans. Magn. **55**, 1 (2019).
[13] O. Safdarzadeh, E. Afjei, and H. Torkaman, Int. J. Appl. Electromagn. Mech. **57**, 257 (2018).
[14] P. Jin, X. He, and Y. Guo, IEEE Trans. Magn. **58**, 1 (2022).
[15] H. Chen, W. Yan, J. J. Gu, and M. Sun, IEEE/ASME Trans. Mechatronics. **23**, 1762 (2018).
[16] W. Zhao, A. Ma, J. Ji, X. Chen, and T. Yao, IEEE. Trans. Ind. Electron. **67**, 80 (2020).
[17] J. Bu, M. Zhou, X. Lan, D. X., and K. X. Lv, IEEE Trans. Magn. **53**, 1 (2017).
[18] A Mahdy, A Shaheen, R El-Sehiemy, A. Ginidi, and S. F. Al-Gahtani, Energies. **16**, 2409 (2023).
[19] Y. Cao, L. Feng, R. Mao, L. Yu, H. Jia, and Z. Jia, Proc. CSEE. **41**, 1983 (2021).
[20] L. Xu, X. Zhu, C. Zhang, and L. Quan, IEEE Trans. Energy Convers. **36**, 3414 (2021).